

RESEARCH OUTPUTS / RÉSULTATS DE RECHERCHE

In-depth investigation of the charge extraction efficiency for thermally annealed inverted bulk-heterojunction solar cells

Kolb, Florian; Busby, Yan; Houssiau, Laurent; J.W. List-Kratchvil, Emil

Published in:
Journal of Applied Physics

DOI:
[10.1063/1.5052409](https://doi.org/10.1063/1.5052409)

Publication date:
2019

Document Version
Peer reviewed version

[Link to publication](#)

Citation for published version (HARVARD):
Kolb, F, Busby, Y, Houssiau, L & J.W. List-Kratchvil, E 2019, 'In-depth investigation of the charge extraction efficiency for thermally annealed inverted bulk-heterojunction solar cells', *Journal of Applied Physics*, vol. 125, no. 3, 034502. <https://doi.org/10.1063/1.5052409>

General rights

Copyright and moral rights for the publications made accessible in the public portal are retained by the authors and/or other copyright owners and it is a condition of accessing publications that users recognise and abide by the legal requirements associated with these rights.

- Users may download and print one copy of any publication from the public portal for the purpose of private study or research.
- You may not further distribute the material or use it for any profit-making activity or commercial gain
- You may freely distribute the URL identifying the publication in the public portal ?

Take down policy

If you believe that this document breaches copyright please contact us providing details, and we will remove access to the work immediately and investigate your claim.

Optimization of the Charge Extraction Efficiency in Inverted Bulk-Heterojunction Solar Cells

Florian Kolb⁽¹⁾, Yan Busby⁽²⁾, Laurent Houssiau⁽²⁾, Emil J.W. List-Kratochvil⁽³⁾

⁽¹⁾ Institute of Surface Technologies and Photonics, JOANNEUM RESEARCH Forschungsges. mbH, Franz-Pichler-Straße 30, 8160 Weiz, Austria

⁽²⁾ Laboratoire Interdisciplinaire de Spectroscopie Electronique, Namur Institute of Structured Matter, University of Namur, 61 Rue de Bruxelles, 5000 Namur, Belgium

⁽³⁾ Institut für Physik, Institut für Chemie & IRIS Adlershof, Humboldt-Universität zu Berlin, Brook-Taylor-Straße 6, 12489 Berlin, Germany

Abstract

The performance of bulk-heterojunction solar cells is significantly affected by several factors among which are the nano-morphology of the photoactive layer and the properties of interfacial layers promoting charge extraction and collection at the electrodes. In this work, we investigate the correlation between the MoO_x layer thickness and the thermal annealing procedure on the device performance and on the charge extraction efficiency of inverted ITO/PEI/P3HT:PCBM/MoO_x/Ag bulk heterojunction solar cells. The surface morphology of pristine and annealed P3HT:PCBM photoactive layers is examined by atomic force microscopy (AFM) before and after the exposure to dichloromethane showing the presence of low-molecular weight and regio-random P3HT domains whose distribution can be related to the applied thermal annealing procedure. The chemical and molecular composition profiles in the photoactive layer and at the interfaces are investigated through depth profile analyses combining X-ray photoelectron spectroscopy and time-of-flight secondary ion mass spectrometry showing a decreasing oxidation gradient of the MoO_x and low diffusion of the

MoO_x species in the P3HT:PCBM layer. Additionally, we show that the voltage dependent photocurrent is significantly affected by non-geminate recombination for devices with a too thin MoO_x layer thickness, while applying a non-optimal thermal annealing procedure leads to an increased geminate recombination mechanism of charge carriers. The highest charge extraction efficiency and device performance is reached for devices with a MoO_x layer above 5 nm while thermal annealing procedure has to be applied before the deposition of the MoO_x/Ag layers.

I. Introduction

Organic bulk-heterojunction solar cell devices (OSCs) have attracted considerable attention in the past decades due to their striking advantages including high versatility for a wide field of different applications, cost-effective fabrication and short energy amortization time. However, to maintain the competitiveness of OSCs, key metrics like the device performance and the long-term stability have to be enhanced on a continuous base. This challenge has been addressed in numerous reports through an improved control of the nanoscale morphology of the photoactive layer forming a bulk heterojunction system (BHJ) and/or through the introduction of interfacial layers to facilitate charge extraction from the photoactive layer.¹⁻⁵ To minimize the electron extraction barrier, typically high work function materials such as calcium⁶, lithium fluoride (LiF)^{7,8} or polyethyleneimine PEI⁹ are used. On the other hand, low work function materials like PEDOT:PSS,^{10,11} tungsten oxide (WO_x)¹² or molybdenum oxide (MoO_x)^{13,14} have been employed to improve the hole extraction. In addition, interfacial layers can act as optical spacers to enhance the optical field of the incident light inside the photoactive layer and thus improving the generation of excitons.^{15,16}

However, the overall device performance in BHJ OSC primarily depends on the morphology of the bi-continuous and interpenetrating network of donor and acceptor materials, as most intensively investigated for poly(3-hexylthiophene) (P3HT) acting as electron donor and the fullerene derivate [6,6]-phenyl-C61-butyric acid methyl ester (PCBM) acting as the electron

acceptor. Yet, in P3HT:PCBM solar cells, as in many other solid state blend systems, post deposition annealing treatments need to be applied to improve the phase separation in the photoactive blend.¹⁷ For this, two approaches have been widely investigated which are called: (i) solvent annealing (i.e exposing the photoactive layer at room temperature to solvent vapors)¹⁸ and (ii) thermal annealing (i.e exposing the photoactive layer to temperatures between 110 and 180 °C). At the same time thermal annealing in presence of interfacial layers or metal electrodes can also lead to severe interdiffusion and to the formation of intermediate layers affecting the charge extraction efficiency and thus the overall solar cell performance. These mechanisms have been reported by several groups in particular for standard P3HT:PCBM/Al devices where thermal annealing in presence of the Al electrode was found to have a beneficial effect on the overall device performance.¹⁹ The comparison between individual solar cell performance indicators obtained for devices annealed prior (pre-annealed) or after (post-annealed) the Al electrode deposition showed an enhanced short circuit current density (J_{SC}) for post annealed devices. This was attributed to a lowered contact resistance between the electrode and the photoactive layer.^{20,21} However, the introduction of an additional interfacial layer between the photoactive blend and the Al electrode may require different thermal annealing procedures. For example, Li *et al.* showed that the performance of P3HT:PCBM/LiF/Al solar cells significantly decreases if thermal annealing is performed after depositing LiF. The device performance decay was caused through a lowered open circuit voltage (V_{OC}) and fill factor (FF) resulting from the LiF diffusing into the photoactive layer which significantly reduced the P3HT crystallinity.²² For inverted device structures, employing MoO_x as interfacial layer, thermal annealing of the photoactive blend is commonly performed before the MoO_x deposition. The influence of post-thermal annealing, where annealing was performed after the deposition of the MoO_x /Ag electrode, was investigated in a previous report.²⁴ It was concluded that the decay of the device performance is due to the loss of cohesion of the MoO_x /Ag interface and consequently the formation of a MoO_x -Ag alloy

interlayer, as well as slight diffusion of the Ag, O and Mo species into the P3HT:PCBM layer. However, this study focused on investigating the MoO_x/P3HT:PCBM interface, while the morphology of the P3HT:PCBM photoactive layer was not examined in detail.

In this work we investigate both the morphology of the P3HT:PCBM photoactive layer and the voltage dependent charge extraction efficiency for devices fabricated following different thermal treatment procedures and bearing MoO_x layer thicknesses from 4 to 12 nm. For the interface analysis, time-of-flight secondary ion mass spectrometry (ToF-SIMS) and X-ray photoelectron spectroscopy (XPS) depth profiles are combined to accurately resolve the in-depth molecular and chemical distributions. In addition, the effect of the thermal treatment sequence on the surface topography of P3HT:PCBM layers was investigated by exposing them to an orthogonal solvent (dichloromethane, DCM) with the intention of dissolving the PCBM without solubilizing the P3HT. The morphological investigations are completed by a discussion of the effects on the voltage dependent photocurrent and the charge extraction efficiency for different MoO_x layer thicknesses and thermal annealing sequences.

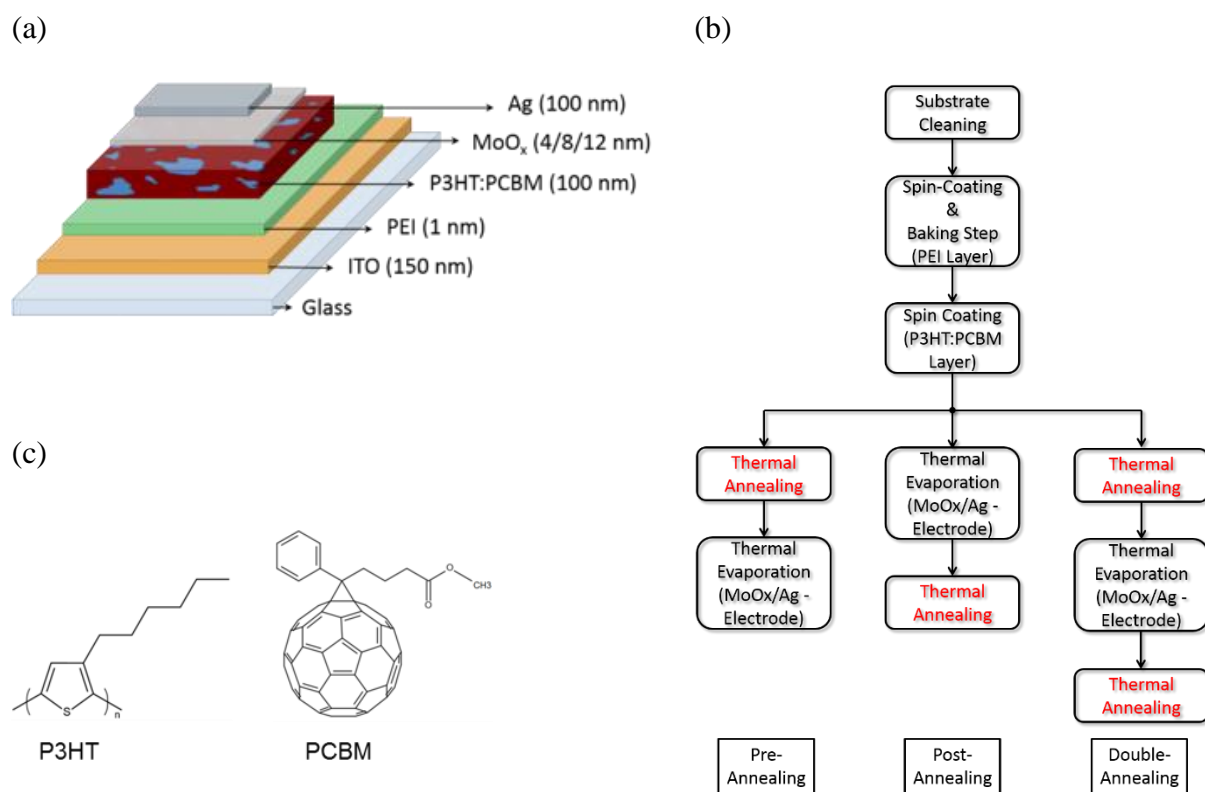


Figure 1: (a) Device structure and respective layer thicknesses of the investigated solar cell device. (b) Fabrication steps associated with the three annealing procedures. (c) Molecular structure of the donor (P3HT) and acceptor (PCBM) species in the photoactive blend.

II. Experimental

A. Materials & Device Fabrication

Regioregular Poly(3-hexylthiophene-2,5-diyl) (P3HT) with a molecular weight $50k < M_w < 70k$ and a regioregularity between 91 and 94% was purchased from Rieke Metals LLC (Reference #4002-E). All solvents (chlorobenzene, 2-butanol, ammonia solution, dichloromethane (DCM)), Phenyl-C61-butyric acid methyl ester (PCBM) and polyethyleneimine (PEI) were purchased from Sigma-Aldrich and used as received. Glass substrates with a pre-patterned ITO layer and a nominal sheet resistance of $15 \Omega/\square$ were obtained from Kintec Company.

Glass/ITO/PEI/P3HT:PCBM/MoO_x/Ag solar cells were fabricated by dissolving P3HT and PCBM compounds in chlorobenzene (20 mg/ml) in a ratio of 1:0.75 (P3HT:PCBM) followed by heating to 75 °C and stirring for 3 h. Subsequently, the blend was cooled down to room temperature and stirred overnight to ensure the complete dissolution of the solid compounds. PEI was dissolved at room temperature under stirring in 2-Butanol to reach a ratio of 0.15 mg/ml. Glass/ITO substrates were cleaned by a standard cleaning procedure consisting of ultrasonication in a diluted Hellmanex bath followed by immersion in acetone and isopropanol baths for 15 min each. Successive fabrication steps were performed in an Ar-filled glovebox where oxygen and water levels were constantly monitored to be below 5 ppm. The PEI solution was spin-coated on the Glass/ITO following a two-step procedure at 1500 rpm for 2 s and 4000 rpm for 20 s. Afterwards, the samples were placed on a hot plate and annealed at 105 °C for 10 min to remove solvent residuals. The P3HT:PCBM solution was spin-coated at 1200 rpm for 80 s leading to the thickness of ~80 nm (as measured on a scratch

in the film). Three different fabrication procedures were realized according to the scheme in **Figure 1b**. The applied temperature and the duration of each thermal annealing treatment was fixed at 150 °C and 15 min. In the *pre (post) annealing* procedure, the thermal treatment is performed before (after) the MoO_x/Ag (~100 nm) deposition by high-vacuum thermal evaporation (base pressure below 1×10⁻⁶ mbar) at the rate of 0.1 Å/s for the MoO_x and 5 Å/s for the Ag layer. For the *double-annealing procedure*, the thermal treatment was applied prior and after the deposition of MoO_x/Ag. The thickness of the MoO_x layer was varied from 4 to 12 nm to optimize the device performance and to correlate charge extraction efficiency with the thickness of the hole transport layer.

B. Surface and Interface Characterizations

Tapping-mode *atomic force microscopy* (AFM, Nanoscope V5 from Veeco) was performed to characterize the surface morphology of spin-coated P3HT as well as P3HT:PCBM layers deposited on Glass/ITO/PEI substrates and exposed to the different thermal annealing treatments. To access the P3HT:PCBM layer surface below the electrodes of fabricated solar cell devices, the MoO_x/Ag was removed by dipping the samples in an ultrasonic NH₃ (30%) bath for 45 s followed by mechanical stripping with an adhesive tape. For the investigations of P3HT and PCBM distributions in pristine or blended films, the samples were placed on a spin coater and DCM was drop-casted on the surface and removed after 10 s by spinning at 4000 rpm for 60 s. Finally, the samples were dried under nitrogen flow and investigated by AFM.

X-ray photoelectron spectroscopy (XPS) depth profile analysis (K-Alpha, Thermo Scientific) was performed by alternating low-energy (500 eV) Ar⁺ sputtering and surface analysis in "snapshot" mode using a monochromatic Al K α X-ray beam, a 400 μ m spot diameter, a raster area of 1.2 mm and dual beam flood gun for charge compensation. The snapshot mode allows for the fast acquisition of core level spectra (Ag 3d, N 1s, C 1s, S 2p, O 1s, I 3d and Mo 3d) with a high resolution within a few minutes. The atomic percentages associated with each

chemical component are evaluated from high-resolution spectra after the peak fitting with Shirley background and using Avantage© software.

Time-of-flight secondary ion mass spectrometry (ToF-SIMS) profiles were acquired with a dual beam ToF-SIMS spectrometer (TOFSIMS IV from Ion-TOF GmbH, Münster, Germany) operated with a 25 keV Bi₃⁺ analysis beam and a 500 eV Cs⁺ ion beam oriented at 45° for sputtering and a flood gun for charge compensation. The acquisition was in negative polarity noninterlaced bunched mode. The analysis area was on 125×125 μm² with a raster area of 250×250 μm².

C. Solar Cell Performance and Charge Extraction Efficiency

The spectral absorbance characteristic of P3HT and P3HT:PCBM layers within the UV-visible range (350-850 nm) was examined by a PERKIN ELMER spectrophotometer (PERKIN ELMER, Lambda 900) equipped with an integrating sphere. Photoluminescence spectra were acquired between 580 and 800 nm on a spectrofluorophotometer (SHIMADZU, RF5301 PC). The wavelength of the excitation source was selected at 517 nm, corresponding to the maximum absorption peak of the P3HT:PCBM layers that were deposited on glass substrates. The J-V characteristics of fabricated solar cells were acquired using a Keithley 2400 coupled with a AM 1.5 calibrated solar simulator (ATLAS Material Testing) providing an irradiance of $P_{inc}=100 \text{ mW/cm}^2$. The solar cell performance is derived through the relation:

$$\eta_P = \frac{V_{MPP}J_{MPP}}{P_{inc}} = \frac{V_{OC}J_{SC}FF}{P_{inc}} ; FF = \frac{V_{MPP}J_{MPP}}{V_{OC}J_{SC}} \quad \text{Eq.(1)}$$

where η_P is the power conversion efficiency (PCE), FF is the fill factor and the MPP index refers to the maximum power point. The open circuit voltage V_{OC} corresponds to the externally applied bias V_{ext} at which under illumination conditions the observed current density is zero, while the short circuit current density J_{SC} is obtained when V_{ext} equals zero. The voltage-dependent charge extraction of investigated devices is correlated to the obtained J-V characteristic by the photocurrent J_{ph} that is defined through the relation:

$$J_{ph} = J_{light} - J_{dark} \quad \text{Eq.(2)}$$

where J_{light} and J_{dark} are the current densities under illumination and dark conditions, respectively. Additionally, we define the charge extraction efficiency by the ratio:

$$\eta_{CEE} = \frac{J_{ph}(V_{eff})}{J_{ph}(V_{eff} = 2.2V)} = \frac{J_{ph}(V_{eff})}{J_{ph}(max)} \quad \text{Eq.(3)}$$

The total internal voltage acting on charge carriers (V_{eff}) corresponds to the externally applied voltage (V_{ext}) corrected by the compensation voltage (V_0) which is the bias where the photocurrent is zero (**Figure 6a**). Plotting J_{ph} vs V_{eff} in log-log scale offers a convenient way to evaluate the power law dependence of the derived photocurrent in relation to the acting effective voltage ($J_{ph} \propto V_{eff}^k$). The experimental linear fit coefficient (k) allows for an identification of different charge transport regimes, i.e. ohmic ($k=1$), saturated ($k=0$) or space charge/recombination limited transport ($k=0.5$).²⁵ In a common approach, two theoretical models are combined to describe the behavior of the voltage dependent photocurrent $J_{ph}(V_{eff})$.^{41,48} The first model developed by Onsager and later extended by Braun in 1984,^{49,50} addresses the dissociation probability of the polaron-pair formed in the photoactive layer upon absorption of an incident photon. Upon successful separation of the polaron-pair and further neglecting trapping and recombination of the free charge carriers, the behavior of $J_{ph}(V_{eff})$ can be related to simulation results obtained from the Sokel-Hughes model.⁵¹

III. Results and Discussion

A. Impact of the thermal treatment sequence on the device performance

Three device sets are investigated to examine the impact of the annealing sequence and the MoO_x layer thickness on the device performance. The current-voltage curves of pre-, post- and double-annealed devices bearing a MoO_x layer thickness (l) of 4, 8 and 12 nm are displayed in **Figure 2** and **Figure S7a** in Supplementary Information. The corresponding average device performance indicators (PCE, FF, V_{OC} , I_{SC}) and the corresponding standard

deviation derived from 16 solar cell devices are summarized in **Table 1**. The highest average PCE of 3.4 % is obtained for $l= 8$ nm and pre-annealing conditions. For $l= 8$ nm post- and double-annealing procedures result in a lower average PCE of 2.5% and 2.1% (-26.5% and -38.2% respectively). By analyzing the other performance indicators, the reduction of the PCE in post and double annealed devices appears to be mainly caused by the significant decrease of J_{SC} (by -23.5% and -36,5%, respectively) while other indicators are almost unaffected by the thermal treatment sequence. Similar results are observed independently from the MoO_x layer thickness (for $l=4$ and $l=12$ nm). The J_{SC} induced decay of the PCE was previously reported for solar cells treated by a thermal aging procedure (ISOS-D2),²⁶ and explained by (i) interface degradation mechanisms or by (ii) the diffusion of the top electrode material into the photoactive blend.²⁷ Since both reasons can explain the decreased J_{SC} observed for post- and double-annealed devices, the morphology of the photoactive blend and the properties of the MoO_x interfacial layer will be carefully investigated in the next section.

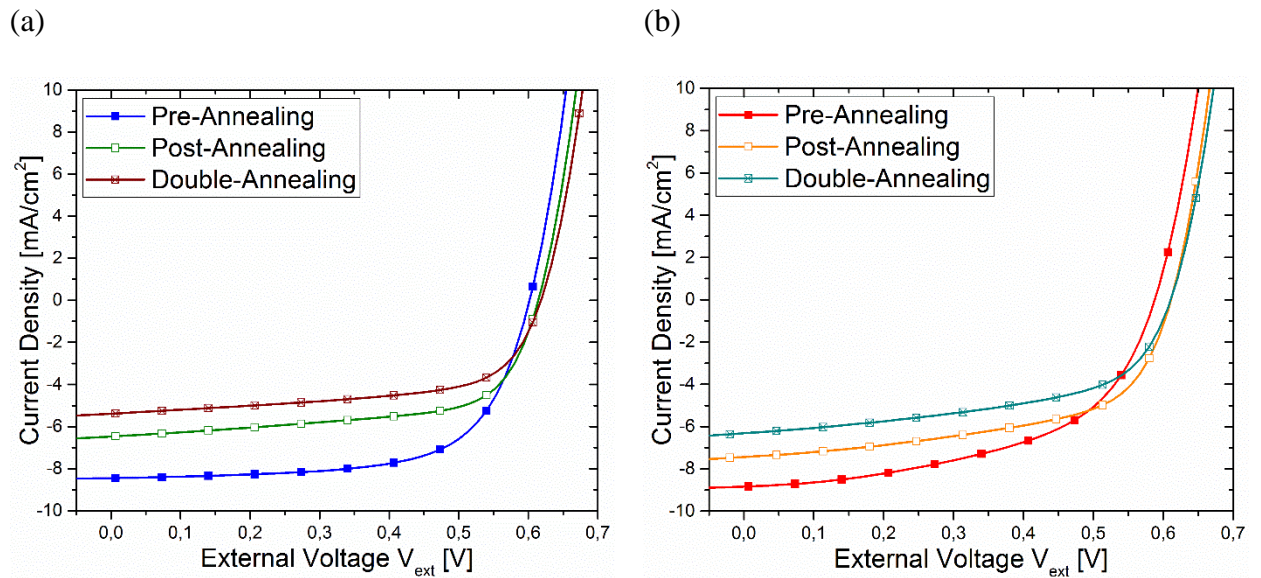


Figure 2. J-V characteristic of investigated device sets subjected to the pre-, post- and double-annealing procedure bearing a MoO_x layer thickness of $l=8$ nm (a) and $l=4$ nm (b).

B. Composition and interface depth profile analyses

In contrast to the general consensus concerning Al diffusion at the P3HT:PCBM/Al interface, previous reports about the P3HT:PCBM/MoO_x interface are much more controversial. Namely, for ITO/MoO₃/P3HT:PCBM/Al devices, MoO_x was shown to diffuse through the whole photoactive layer,²³ while this behavior was not observed for Glass/ITO/TiO_x/P3HT:PCBM/MoO_x/Ag devices.²⁴ To assess the potential diffusion of Mo and/or MoO_x related species in the devices fabricated following our three annealing procedures, the chemical composition of the MoO_x layer was investigated by XPS and ToF-SIMS depth profiling. XPS profiles were made with low energy (500 eV) Ar⁺ sputtering and ToF-SIMS with low-energy Cs⁺ in order to limit sputtering induced artifacts and preserve the device interfaces.^{28,29} The accurate peak fitting of Mo 3d core level spectra acquired at different sputtering times (i.e. depths) evidence a variable in-depth chemical composition of the MoO_x layer with a more oxidized (~MoO₃) state at the Ag/MoO_x interface and a less oxidized layer (~MoO) at the MoO_x/P3HT:PCBM interface (**Figure 3a** and **3b**). Interestingly, the depth evolution of the MoO_x layer chemical composition was almost identical for the devices subjected to the pre- or double-annealing procedures (**Figure 3c** and **3d** and **Figure S5**). To improve the detection limit with respect to XPS analysis (~0.1 atomic %) and more safely exclude that the depth-dependent MoO_x layer composition variation is the result of the preferential sputtering of oxygen species by the low-energy Ar⁺ beam.^{30,31}

ToF-SIMS depth profiles were performed with low-energy Cs⁺ beam on pre- (**Figure 4**) or double-annealed (**Figure S6**) devices. From the comparative analysis of MoO⁻, MoO₂⁻ and MoO₃⁻ molecular signals profiles (note that each fragment is characterized by its specific ionization yield) in pre- and double-annealed devices, we clearly observe perfectly similar features, i.e. (i) a negligible diffusion of MoO_x across the P3HT:PCBM, (ii) the presence of the three oxidation states in agreement with XPS results and (iii) that the thermal annealing procedure does not sensibly affect the MoO_x layer composition. From this clear experimental

results we can safely assess that the performance differences in the solar cells exposed to different thermal annealing schemes are not ascribed to differences in the MoO_x layer composition or by interdiffusion effects at the P3HT:PCBM/ MoO_x interface.

The use of low energy sputtering beams allows limiting although not completely excluding preferential sputtering of oxygen (i.e. the reduction of MoO_x species); however, the oxidation profile is mainly ascribed to the high-vacuum thermal evaporation process of the MoO_3 precursor, namely by the possibly different sticking coefficients of oxygen and Mo atoms on the BHJ surface.³²

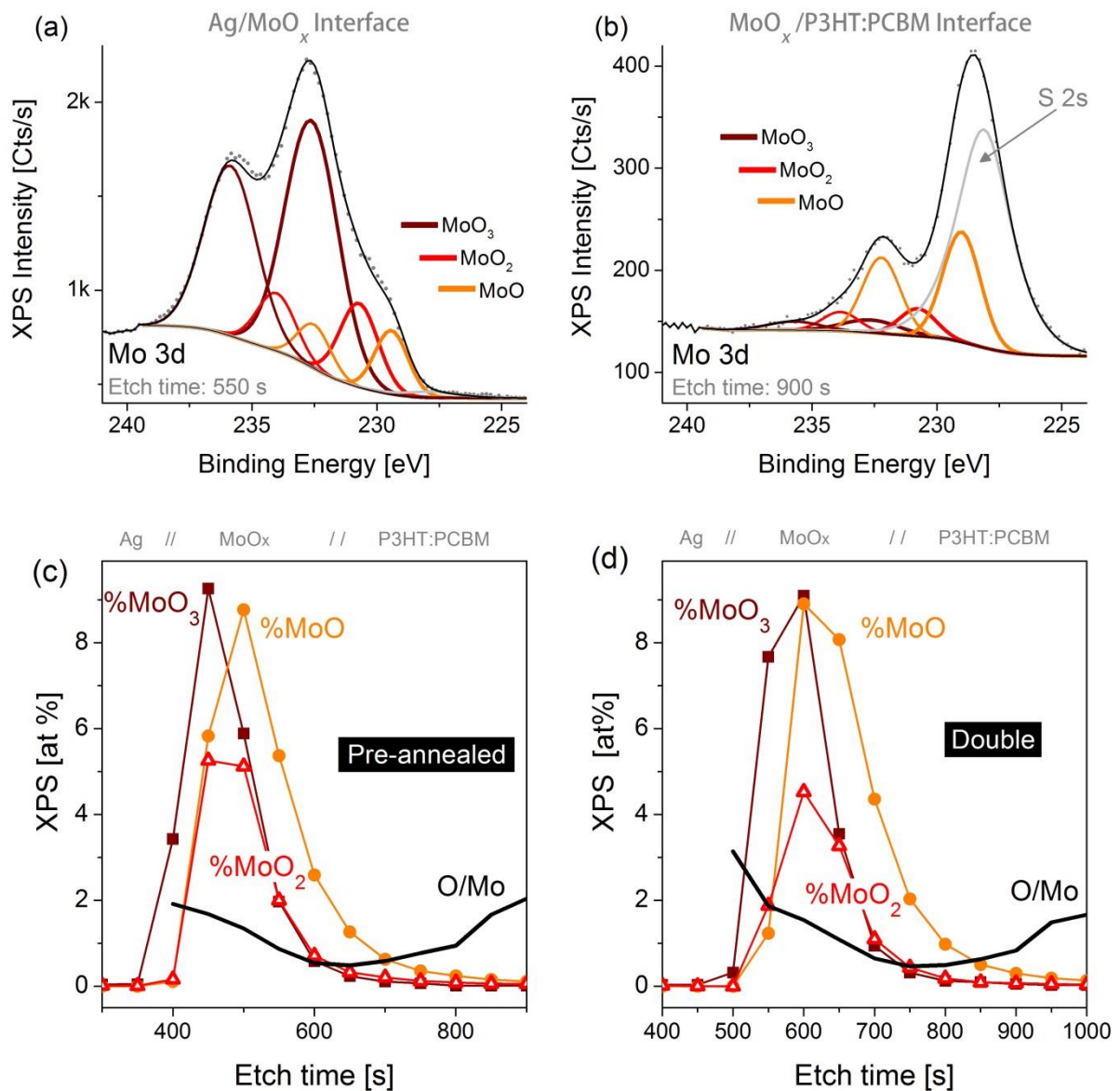


Figure 3. Fitting procedure of the XPS Mo 3d spectra acquired at different depths for a double-annealed device. Different oxidation states of molybdenum are found at the upper (Ag/MoO_x) interface (a) and at the lower (MoO_x/P3HT:PCBM) interface (b). XPS depth profiles with 500 eV Ar⁺ sputtering beam show very similar Mo layer chemical composition profiles in solar cells subjected to pre- (c) or double-annealing (d) procedures.

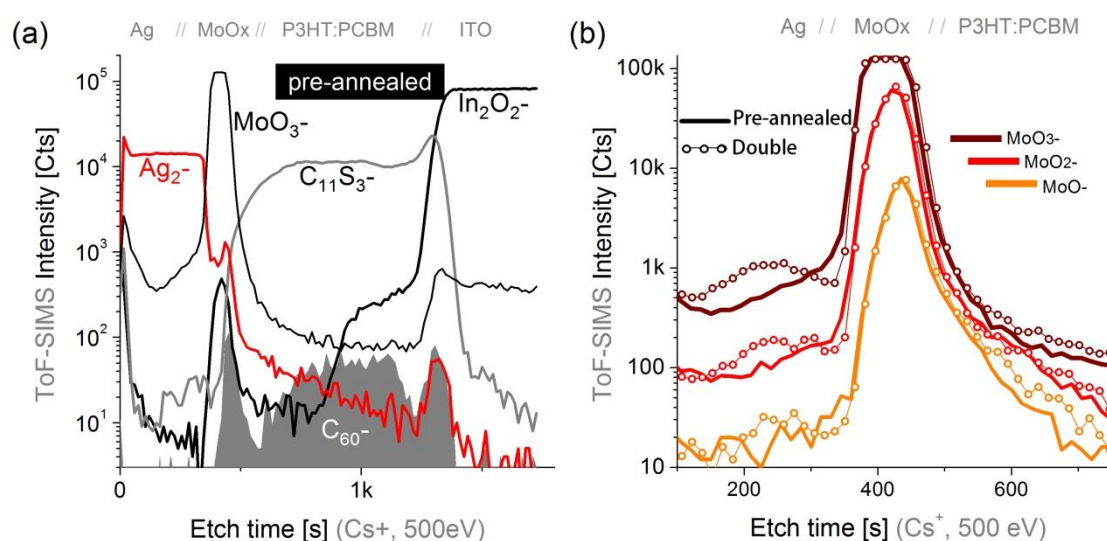


Figure 4. (a) ToF-SIMS depth profiles obtained on device fabricated following the pre-annealing scheme. (b) Comparison between MoO⁻, MoO₂⁻ and MoO₃⁻ molecular signals derived from pre- or double-annealed devices.

C. Influence of the thermal annealing sequence on the bulk heterojunction morphology

The P3HT:PCBM BHJ morphology was characterized in devices bearing the same MoO_x layer thickness (*l*=8 nm) but treated by different thermal annealing procedures. AFM topography and phase images did not reveal any significant annealing procedure (see **Figure S1** and **S3** in Supplementary Information). Moreover, the associated phase images do not allow distinguishing between the individual components of the photoactive layer to eventually evidence phase separation within the photoactive layer (**Figure S1**). It was previously

reported that prolonging the annealing time resulted in the enhancement of the vertical segregation of the PCBM phase and possibly lead to the formation of μm -sized PCBM aggregates which considerably increased the charge recombination rate.^{33–38} In our case, since PCBM aggregates are not observed at the BHJ surface, maybe because of the too short annealing time, we considered an alternative approach consisting of washing the BHJ film with dichloromethane (DCM) in order to dissolve PCBM without affecting the P3HT morphology. Therefore, we expected the appearance of cavities in the film morphology corresponding to PCBM-rich phases. To confirm the successful removal of the PCBM species from the P3HT:PCBM layer following the DCM treatment, we performed photoluminescence and absorbance investigations. Regardless of the thermal annealing procedure, the photoluminescence and the absorbance properties of DCM washed P3HT:PCBM layers are similar to those observed for a pristine P3HT layer (i.e. without PCBM, see **Figure 5a** and **5b**). The suppression of the quenching effect from PCBM is a clear indication of the PCBM removal by DCM. In addition, the absorbance spectrum of pristine P3HT layers does not change upon DCM treatment (shown in **Figure S2** in Supplementary Information), confirming that the bulk of the P3HT is not affected by the solvent treatment, whereas the absorbance spectra of P3HT:PCBM layers differs significantly from pristine P3HT films. (see inset-graph in **Figure 5b**).

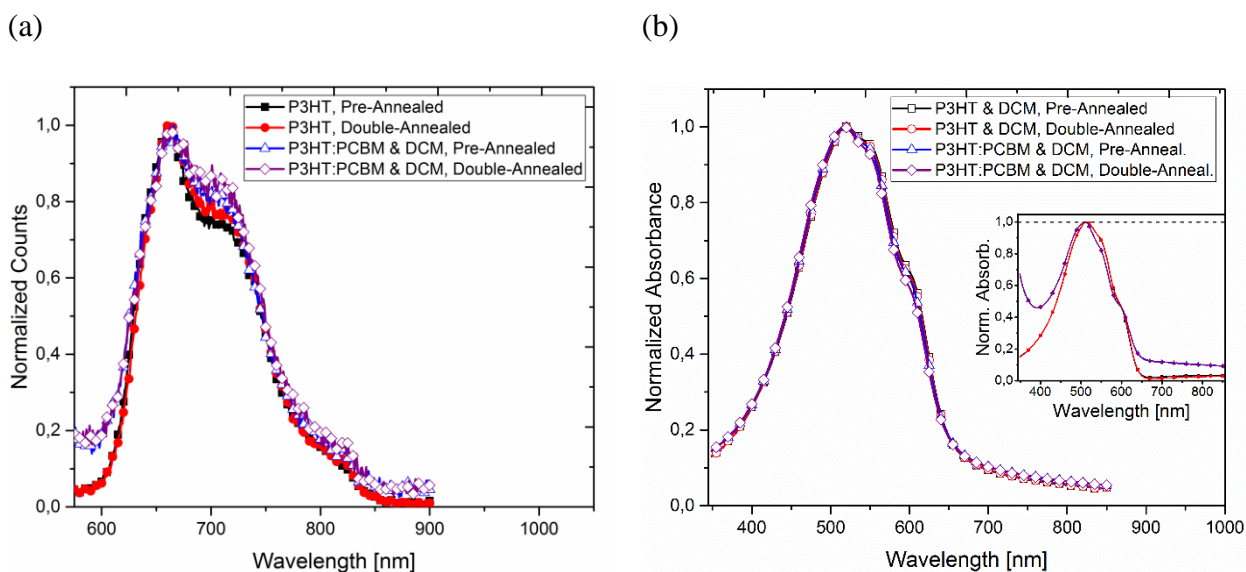


Figure 5. (a) Fluorescence spectra from P3HT, P3HT:PCBM and DCM-treated P3HT:PCBM layers subjected to the pre- or double-annealing procedure. (b) Absorbance spectra of DCM washed P3HT and P3HT:PCBM layers subjected to the pre- or double-annealing procedures. The inset-graph shows the absorbance spectra of thermally annealed P3HT and P3HT:PCBM layers before DCM treatment.

We further investigated by AFM the surface morphology of P3HT:PCBM films subjected to the different thermal annealing procedures and to the DCM treatment. The AFM images are taken both at open areas between the electrodes (see **Figure 6a-c**) and underneath the electrodes (see Supplementary Information **Figure S4**). For both regions and regardless of the applied thermal annealing procedure, the DCM treatment results in the appearance of cavities, whose density is significantly higher in post- and double- annealed devices. For these devices, we observe an almost uniform dense distribution of sub-micrometer scale cavities, while in pre-annealed devices, only few sparse micrometer scale cavities are observed (see **Figure 6a-c**). To investigate the origin of these cavities and to discriminate whether they can be correlated to the removal of PCBM-rich phases, pristine P3HT films were also annealed and washed with DCM in a similar manner as the P3HT:PCBM layers. Surprisingly, and regardless of the thermal annealing procedure, the cavities in DCM washed P3HT are very

similar than the ones observed at P3HT:PCBM films (see **Figure 6d-f**). This leads us to the conclusion that the cavities appearing following DCM treatment originate from the partial removal of P3HT domains. Previous reports focusing on the solubility of P3HT in DCM evidenced that high- M_w P3HT (as used within this study) is almost insoluble in DCM while regio-random and low- M_w P3HT impurities can be solubilized by DCM washing.^{39,40} In summary, we observe a clear difference between the three differently annealed and DCM washed P3HT:PCBM samples. However, the occurrence of the DCM-induced cavities in P3HT:PCBM films cannot be exclusively related to the removal of PCBM as shown by the outcome of the control experiments where pristine P3HT layers were treated with DCM. To correlate the results obtained from our morphological investigation to the key performance indicators of solar cells, the behavior voltage dependent photocurrent in dependence of the applied thermal annealing procedure and the MoO_x layer thickness is discussed in the following section.

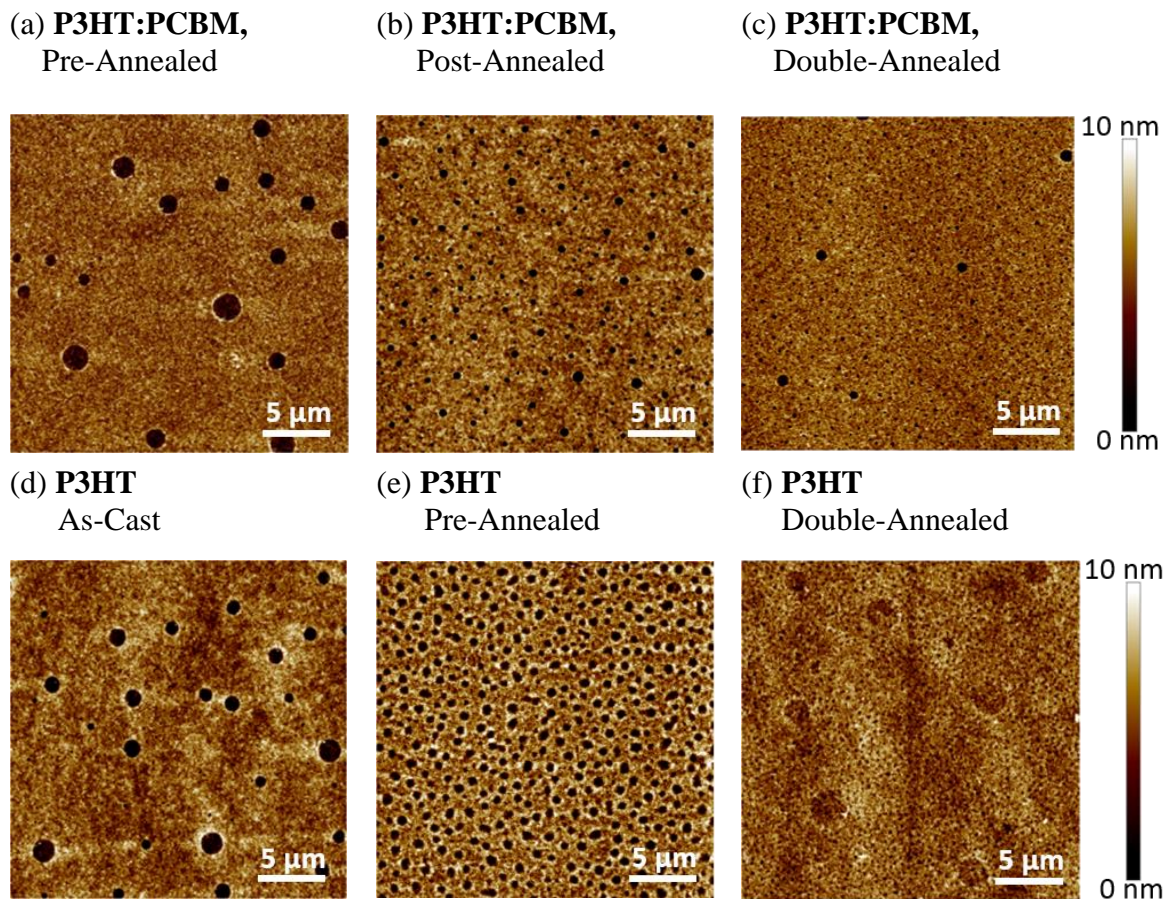


Figure 6: AFM topography images of annealed P3HT:PCBM (a-c) and P3HT (d-f) films exposed to DCM. Images (a), (b) and (c) are acquired in regions between the metal electrodes.

D. Impact of the thickness of the MoO_x layer and the thermal treatment procedure on the charge extraction

Since neither the interface depth profiles nor the morphological characterization could give valuable information to derive structure-to-performance relationships in solar cells, we characterized the charge extraction regimes by the conventional approach of plotting photocurrent-effective voltage (J_{ph} - V_{eff}) curves in a double-logarithmic scale.

We firstly restrict our discussions on pre-annealed solar cells bearing different MoO_x layer thicknesses. The effects of the MoO_x layer thickness on the overall device performance has been extensively investigated by a number of different approaches, including fitting of the obtained JV curve to an equivalent electrical circuit model. In this case, for a MoO_x layer

thicknesses < 3 nm the low device performance, caused by a decreased V_{OC} , J_{SC} and FF, was ascribed to an increased series resistance and/or by a decreased shunt resistance.^{43,44}

Investigating the effect of a varied MoO_x layer thickness on the voltage dependent photocurrent shows for small $V_{eff} < 0.1$ V an ohmic transport regime (i.e. $J_{ph} \propto V_{eff}^k$ with $k=1$), while increasing $V_{eff} > 0.2$ V leads to saturation of the photocurrent ($k=0$) as shown in **Figure 7**. A similar trend of the photocurrent is observed for both $l=8$ nm and $l=12$ nm, whereas J_{ph} is slightly lowered for devices bearing a higher MoO_x layer thickness than 8 nm. The shape of the extraction efficiency, which we define by normalizing the photocurrent $J_{ph}(V_{eff})$ to the photocurrent observed at $V_{eff} = 2.2$ V (see **Eq. 3**), is in good agreement with results obtained from the Sokel-Hughes model showing a linear increase for small V_{eff} and saturation of J_{ph} for high effective voltages. Thus, for pre-annealed devices with $l \geq 8$ nm recombination and trapping mechanisms are apparently not affecting charge extraction. However, for $l=4$ nm, $J_{ph}(V_{eff})$ differs significantly within $0.2 < V_{eff} < 0.5$ V and saturation of the photocurrent is only observed when increasing $V_{eff} > 0.5$ V. An exponent of $k \sim 0.3$ was derived for $0.2 < V_{eff} < 0.5$ V, which does not allow for an association with space charge or recombination limited transport regimes as this would require an exponent $k=0.5$.^{25,41,42} The effective voltage V_{eff} acting on charge carriers within a device can be understood in general as the sum of the applied external voltage and the built-in voltage V_{bi} which depends on the HOMO and LUMO level of the donor and acceptor material as well as on the work function of the electrode materials.⁵¹ In a previous report, investigating the development of the work function in relation to the film thickness for metal oxide layers, it was shown that the work function of metal oxides become stable only above a certain layer thickness; for MoO_x a critical thickness of $l=5$ nm was derived.⁴⁶ Hence, for devices bearing a MoO_x layer thickness below this critical value an energy level mismatch is observed between the HOMO energy level of P3HT and the MoO_x work function. As a consequence, such devices require a larger effective voltage to reach saturation of the photocurrent while for small V_{eff} the charge

extraction efficiency is affected by surface recombination due to the lower charge selectivity of the anode.⁴⁵

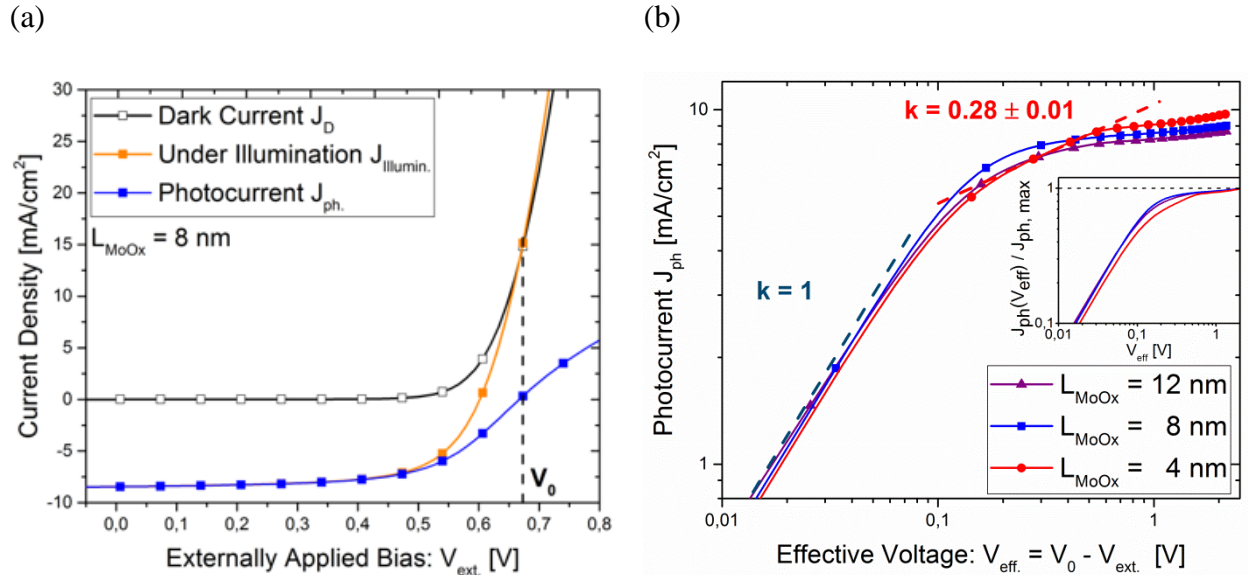


Figure 7. (a) $J_{\text{Ph}}-V_{\text{eff}}$ curves obtained for the pre-annealed solar cell devices (with $l=8$ nm) showing the derived photocurrent (J_{Ph}) and the compensation voltage (V_0). (b) Comparison between the J_{Ph} characteristics for pre-annealed solar cells differing by the respective MoO_x layer thickness ($l=4, 8$ or 12 nm). The exponent k derived from the exponential relation $J_{\text{ph}} \sim V_{\text{eff}}^k$, is indicated by dashed lines. For devices with a MoO_x layer thickness > 8 nm the voltage-dependent charge extraction efficiency shows a similar exponential relationship on the effective voltage as high-lighted at the inset graph in (b).

In the following, the voltage dependent charge extraction efficiency is discussed as a function of the thermal annealing procedure. The comparison between the voltage dependent charge extraction efficiency defined as the ratio of $J_{\text{ph}}(V_{\text{eff}})$ to $J_{\text{ph}}(\text{max}, V_{\text{eff}} = 2.2)$ observed for pre-annealed devices is given in **Figure 8a** and **Figure 8b** for devices with $l= 4, 8$ nm; for devices with $l= 12$ nm see **Figure S7** in Supplementary Information. With respect to pre-annealed devices, post- and double-annealed solar cells feature an overall lower photocurrent

for $V_{\text{eff}} > 0.1$ V. Furthermore, the photocurrent does not saturate for $V_{\text{eff}} > 0.3$ V, but rather increases with a constant exponent $k \sim 0.2$. Hence, for post- and double annealed devices a higher internal field (i.e. V_{eff}) is needed to sweep out light-generated charges and to reach the saturation regime. Moreover, a similar behavior of the charge extraction efficiency for $V_{\text{eff}} > 0.6$ V is observed independently of the MoO_x layer thickness for post and double-annealed devices, as shown in **Figure 8c** and **Figure 8d**.

The dependence of the derived light-generated photocurrent with respect to different magnitudes of the effective voltage has been investigated by Mihailetschi *et. al.*,⁴¹ showing that for small effective voltages J_{ph} can be described by the model proposed by Sokel and Hughes,⁵¹ while for large V_{eff} the behavior of the photocurrent becomes governed by the dissociation probability of the polaron pairs which was developed by Onsager and extended later by Braun.^{49,50} In a different approach based on fundamental statistics of fermions it was shown that non-geminate recombination dominate when $V \sim V_{\text{OC}}$ (i.e small V_{eff}) while geminate recombination dominates at low applied voltages ($V \sim 0$ V, or $V_{\text{eff}} > 0.4$ V), i.e at high internal electric field.⁴⁷ Hence, for the pre-annealed solar cell with $l=4$ nm, the extraction of light-generated charges is mainly limited by non-geminate recombination of (free) charge carriers at the anode that can be suppressed by increasing the MoO_x layer thickness. In contrast, for post- and double-annealed devices the behavior of the photocurrent cannot be related to the MoO_x thickness for $V_{\text{eff}} > 0.6$ V and thus the charge extraction efficiency is mainly limited by geminate recombination that can be only overcome by increasing the effective voltage. In the following section we will show how the individual performance indicators (V_{OC} , FF and J_{SC}) are affected by the different recombination mechanisms.

(a)

(b)

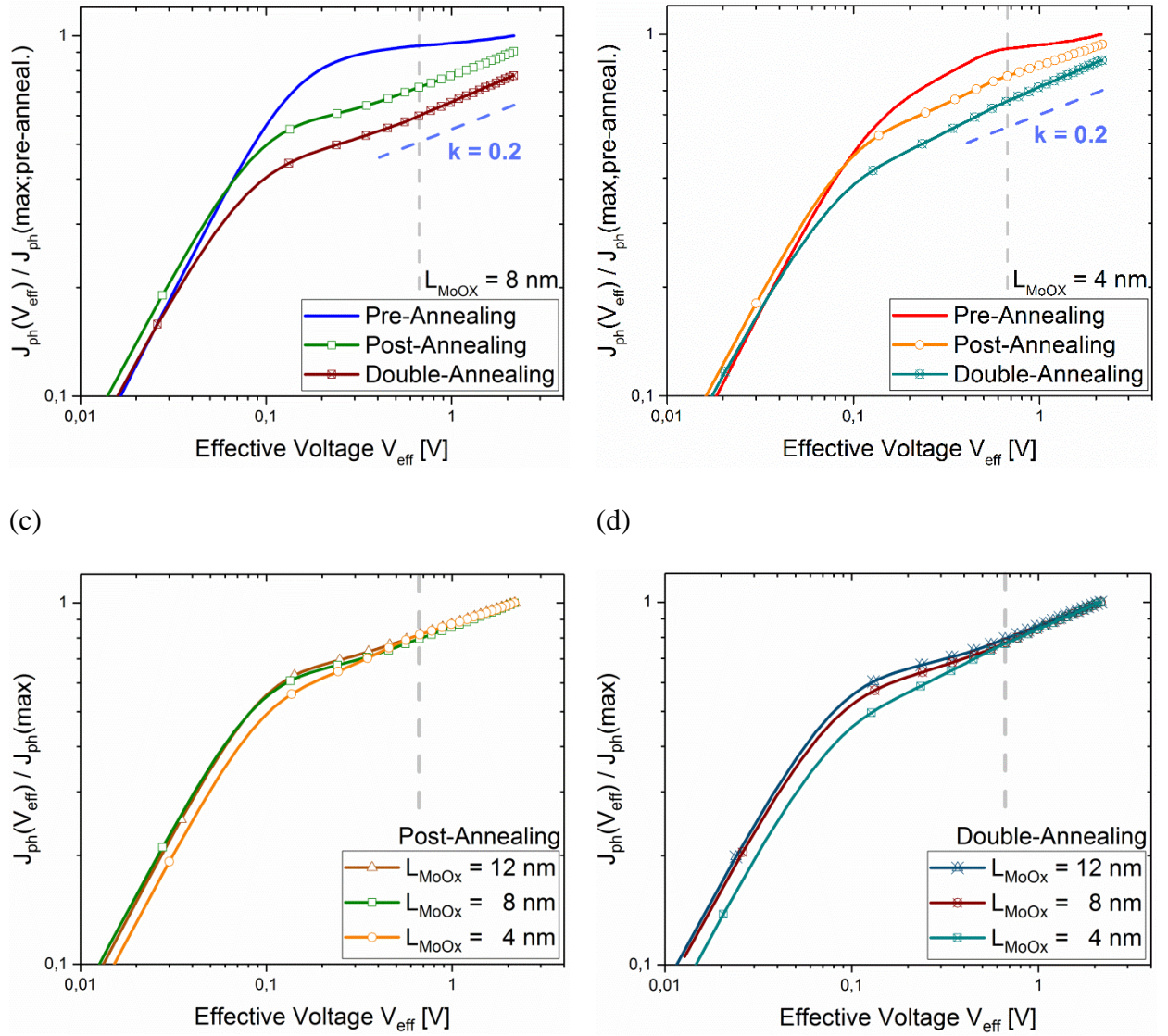


Figure 8. Charge extraction efficiency of post- and double annealed solar cell devices compared to pre-annealed devices with a MoO_x layer thickness $l=8$ nm (a) and $l=4$ nm (b). For post- and double-annealed devices the behavior of the charge extraction efficiency differs in dependence of the MoO_x layer thickness for small V_{eff} but becomes similar for $V_{\text{eff}} > 0.6$ V (c, d). Dashed lines correspond to the linear fit values used to evaluate the power law k ($J_{\text{ph}} \sim V_{\text{eff}}^k$). Vertical dashed lines indicate the bias where V_{eff} equals to $V_{\text{ext}} = 0$ V.

E. Influence of the MoO_x layer thickness and the annealing procedure on the solar cell performance indicators

The results obtained from the $J_{\text{ph}}-V_{\text{eff}}$ curves allow for a rigid interpretation of the evolution of individual performance indicators with the MoO_x layer thickness and the annealing procedure. The optimum conditions giving the best performance ($\eta_{\text{p}} = 3.4 \pm 0.2 \%$, $J_{\text{SC}} = 8.5 \pm 0.1 \text{ mA/cm}^2$ and $\text{FF} = 0.66 \pm 0.3$), correspond to pre-annealed devices with $l=8 \text{ nm}$. This result is in good agreement with our observations of the voltage dependent charge extraction efficiency, which showed an ohmic behavior for $V_{\text{eff}} < 0.1$ while becoming saturated for $V_{\text{eff}} > 0.2 \text{ V}$. However, for devices with a lower MoO_x layer thickness ($l=4 \text{ nm}$), the J_{SC} increases by 3.5% but the FF decreases by -19.7 %, resulting in a significantly lowered PCE (-18%). Increasing the MoO_x thickness ($l=12 \text{ nm}$) results also in a drop of the FF (-6.1%) and to a reduction of J_{SC} (-4.7%). The drop of FF is ascribed to the different behavior of the charge extraction efficiency within $0.1 \text{ V} < V_{\text{eff}} < 0.3 \text{ V}$ (see **Figure 7b**). This effective voltage interval corresponds to an external voltage range of $0.6 \text{ V} < V_{\text{ext}} < 0.4 \text{ V}$ and thus to the interval where FF is derived (see **Eq. 1**). Interestingly, we find J_{SC} increased for $l=4 \text{ nm}$ but an opposite trend for devices with $l > 8 \text{ nm}$ and which cannot be explained by the behavior of the voltage dependent charge extraction efficiency. In agreement with previous reports we attribute the different behavior of J_{SC} in dependence of the MoO_x thickness to different series and shunt resistance of each respective device, where both resistors were acquired through fitting of the JV curve to an equivalent circuit model.^{23,26,43} The J_{SC} reduction observed for post- and double-annealed solar cells and regardless of l , is a consequence of the J_{ph} suppression for $V_{\text{eff}} > 0.1 \text{ V}$ which can be explained by geminate charge recombination due to a significantly lowered polaron pair dissociation probability.

To sum up, our results indicate the necessity of accurately optimizing the MoO_x layer thickness and the annealing-procedure for maximizing the charge carrier extraction efficiency and reducing geminate and non-geminate charge recombination. Moreover, the final J_{SC} and

the FF values are affected differently by varying the MoO_x layer thickness or the annealing procedure as indicated by the charge recombination mechanism occurring in different voltage intervals.

Table 1. Derived performance indicators of solar cells with different MoO_x layer thicknesses (*l*) and thermal annealing procedures. Presented results are the average and the standard deviation derived from 16 cells for each individual case.

Annealing procedure	V _{oc} [V]	J _{sc} [mA/cm ²]	FF	η _p [%]
<i>l</i>=4 nm				
Pre-Annealing	0.59 ±0.01	8.8 ± 0.1	0.53 ± 0.03	2.8 ±0.2
Post-Annealing	0.61 ±0.01	7.4 ± 0.1	0.57 ± 0.01	2.6 ±0.2
Double-Annealing	0.61 ±0.01	6.3 ± 0.1	0.54 ± 0.01	2.1 ± 0.1
<i>l</i>=8 nm				
Pre-Annealing	0.60 ±0.01	8.5 ± 0.1	0.66 ± 0.03	3.4 ± 0.2
Post-Annealing	0.61 ±0.01	6.5 ± 0.1	0.63 ± 0.03	2.5±0.2
Double-Annealing	0.62 ±0.01	5.4 ± 0.1	0.62 ± 0.02	2.1± 0.1
<i>l</i>=12 nm				
Pre-Annealing	0.60 ±0.01	8.1 ± 0.1	0.62 ± 0.03	3.0 ± 0.2
Post-Annealing	0.62 ±0.01	6.4 ± 0.5	0.64 ± 0.02	2.5 ± 0.3
Double-Annealing	0.62 ±0.01	6.0 ± 0.6	0.64 ± 0.02	2.3 ± 0.3

IV. Conclusion

The effect of the MoO_x layer thickness and the thermal annealing procedure on the performance and charge extraction efficiency has been investigated for the inverted ITO/PEI/P3HT:PCBM/MoO_x/Ag solar cell structure. In addition, the photoactive layer morphology was examined through an original approach combining DCM treatment and AFM analysis. Absorbance and photoluminescence measurements have proved the successful PCBM removal upon DCM treatment and AFM analysis has shown the formation of circular-shaped cavities which were ascribed to the partial dissolution of low-M_w and regio-random P3HT domains present at the BHJ surface. The in-depth chemical and molecular composition of the MoO_x layer and its interfaces, characterized by XPS and ToF-SIMS, shows the presence of a gradient Mo oxidation profile, with a more oxidized layer (~MoO₃) at the MoO_x/Ag interface and a less oxidized state (~MoO) at the P3HT:PCBM/MoO_x interface possibly due to the different sticking coefficient of oxygen and molybdenum species. Interestingly, neither the MoO_x oxidation profile nor the (weak) diffusion of the MoO_x species in P3HT:PCBM are influenced by the thermal annealing procedure. Log-log J_{ph}-V_{eff} curves were analyzed to identify the different charge extraction regimes by the respective power law fit coefficient k ($J_{ph} \sim V_{eff}^k$). For the best performing solar cells (pre-annealing and $l=8$ nm) an ohmic regime ($k=1$) is observed at $V_{eff} \sim V_{OC}$ followed by a saturation regime ($k=0$) at $V_{eff} > 0.3$ V indicating an optimal carrier sweepout. The reduction of the MoO_x layer thickness introduces an intermediate charge extraction regime ($k=0.28$) at $0.2 < V_{eff} < 0.5$ V. In post- or double-annealed solar cells, a similar regime (with $k \sim 0.2$) is observed for $V_{eff} > 0.4$ V. Intermediate charge extraction regimes occur in different effective voltage ranges, indicating for different charge recombination mechanisms and well-explain the J_{sc} and FF reduction for non-optimized process conditions. The results clearly indicate that exceeding a minimum MoO_x layer thickness (~5 nm) and application of an optimized thermal annealing procedure

(here by the pre-annealing scheme) is mandatory to maximize the charge extraction efficiency and thus the overall solar cell performance.

Supporting Information

The supporting information provides additional experimental results, including AFM images for regions below the electrodes, absorbance spectra, XPS depth profiles, TOF-SIMS depth profiles and JV curves.

Acknowledgement

F.K. would like to acknowledge the financial support from FWF through the project PLASMOSOL (TRP-304-N20). Franz Peter Wenzl and Mirella El Gemayel are gratefully acknowledged by F.K. for fruitful discussions and proofreading the manuscript.

- ¹ A. J. Moulé and K. Meerholz, “Morphology Control in Solution-Processed Bulk-heterojunction Solar Cell Mixtures,” *Adv. Funct. Mater.* **19**, 3028–3036 (2009).
- ² Y. Huang, E. J. Kramer, A. J. Heeger and G. C. Bazan, “Bulk Heterojunction Solar Cells: Morphology and Performance Relationships,” *Chem. Rev.* **114**, 7006–7043 (2014).
- ³ B. Ray, P. R. Nair and M. A. Alam, “Unraveling the Role of Morphology on Organic Solar Cell Performance,” vol. 47906, pp. 1–10.
- ⁴ R. Steim, F. R. Kogler and C.J. Brabec, “Interface Materials for Organic Solar Cells,” *J. Mater. Chem.* **20**, 2499 (2010).
- ⁵ H. Zeng, X. Zhu, Y. Liang and X. Guo, “ Interfacial Layer Engineering for Performance Enhancement in Polymer Solar Cells,” *Polymers* **7**, 333–372 (2015) .

- ⁶ W. H. Tseng, M. H. Chen, J. Y. Wang, C. T. Tseng, H. Lo, P. S. Wang, C. I. Wu, “Investigations of Efficiency Improvements in Poly(3-Hexylthiophene) Based Organic Solar cells Using Calcium Cathodes,” *Sol. Energ. Mat. Sol. Cells* **95**, 3424–3427 (2011).
- ⁷ C. J. Brabec, S. E. Shaheen, C. Winder, N. S. Sariciftci and P. Denk, “Effect of LiF/Metal Electrodes on the Performance of Plastic Solar Cells,” *Appl. Phys. Lett.* **80**, 1288–1290 (2002).
- ⁸ S.-J. Lee, S. Jeong, D.-H. Kim, C. Kim and Y.-S. Han “Inverted Polymer Solar Cells with an Ultrathin Lithium Fluoride Buffer Layer,” *J. Nanosci. Nanotechnol.* **12**(4), 3205–3209 (2012).
- ⁹ Y. Udum, P. Denk, G. Adam, D.H. Apaydin, A. Nevsad, C. Teichert, M.S. White, N.S. Sariciftci and M.C. Scharber, “Inverted Bulk-Heterojunction Solar Cell with Cross-Linked Hole-Blocking Layer,” *Org. Electron.* **15**, 997–1001 (2014).
- ¹⁰ K. Sun, S. Zhang, P. Li, Y. Xia, X. Zhang, D. Du, F.H. Isikgor and J. Ouyang, “Review on Application of PEDOTs and PEDOT:PSS in Energy Conversion and Storage Devices,” *J. Mater. Sci.: Mater. Electron.* **26**, 4438–4462 (2015).
- ¹¹ F. Ongul, S.A. Yuksel, M. Kazici, S. Bozar, A. Gunbatti and S. Gunes, “Effects of Different Formulation PEDOT:PSS Hole Transport Layers on Photovoltaic Performance of Organic Solar Cells,” *Polym. Adv. Technol.* **28**, 947–951 (2017).
- ¹² C. Tao, S. Ruan, G. Xie, X. Kong, L. Shen, F. Meng, C. Liu, X. Zhang and W. Chen, “Role of Tungsten Oxide in Inverted Polymer Solar Cells,” *Appl. Phys. Lett.* **94**, 043311 (2009).

- ¹³ D. Y. Kim, J. Subbiah, G. Sarasqueta, F. So, H. Ding, Irfan and Y. Gao, "The Effect of Molybdenum Oxide Interlayer on Organic Photovoltaic Cells," *Appl. Phys. Lett.* **95**, 093304 (2009).
- ¹⁴ C. Tao, S. Ruan, X. Zhang, G. Xie, L. Shen, X. Kong, W. Dong, C. Liu and W. Chen, "Performance Improvement of Inverted Polymer Solar Cells with Different Top Electrodes by Introducing a MoO₃ Buffer Layer," *Appl. Phys. Lett.* **93**, 2008–2010 (2008).
- ¹⁵ J. Y. Kim, S. H. Kim, H.H. Lee, K. Lee, W. Ma, X. Gong and A. J. Heeger, "New Architecture for High-Efficiency Polymer Photovoltaic Cells Using Solution-Based Titanium Oxide as an Optical Spacer," *Adv. Mater.* **18**, 572–576 (2006).
- ¹⁶ Y. Zhang, A. K. Pandey, C. Tao, Y. Fang, H. Jin, P. L. Burn and P. Meredith, "Spectral Response Tuning Using an Optical Spacer in Broad-Band Organic Solar Cells," *Appl. Phys. Lett.* **102**, 013302 (2013).
- ¹⁷ M. Campoy-Quiles, M. Schmidt, D. Nassyrov, O. Peña, A. R. Goñi, M. I. Alonso and M. Garriga, "Real-Time Studies During Coating and Post-Deposition Annealing in Organic Semiconductors," *Thin Solid Films* **519**, 2678–2681 (2011).
- ¹⁸ A. J. Pearson, T. Wang, D. G. Lidzey, "The Role of Dynamic Measurements in Correlating Structure with Optoelectronic Properties in Polymer : Fullerene Bulk-Heterojunction Solar Cells," *Rep. Prog. Phys.* **76**, 022501 (2013).
- ¹⁹ H. J. Kim, J. H. Park, H. H. Lee, D. R. Lee and J. J. Kim, "The Effect of Al Electrodes on the Nanostructure of Poly(3-Hexylthiophene): Fullerene Solar Cell Blends During Thermal Annealing," *Org. Electron.* **10**, 1505–1510 (2009).

- ²⁰ G. Li, V. Shrotriya, Y. Yao, Y. Yang, “Investigation of Annealing Effects and Film Thickness Dependence of Polymer Solar Cells Based on Poly(3-Hexylthiophene),” *J. Appl. Phys.* **98**, 043704 (2005).
- ²¹ N. Rujisamphan, F. Deng, R. E. Murray, C. Ni and S. Ismat Shah, “Focused Ion Beam Assisted Investigations of Al Interface in Polythiophene:Fullerene Solar Cells,” *Sol. Energy Mater Sol. Cells* **109**, 56–62 (2013).
- ²² F. Li, J. Zhao, K. Yao and Y. Chen, “Origin of the Efficiency Improvement in Pre-Annealed P3HT/PCBM Solar Cells with LiF/Al Electrodes,” *Chem. Phys. Lett.* **553**, 36–40 (2012).
- ²³ M. Nyman, S. Dahlström, O. J. Sandberg and R. Österbacka, “Unintentional Bulk Doping of Polymer-Fullerene Blends from a Thin Interfacial Layer of MoO₃,” *Adv. Energy Mater.* **6**, 1600670 (2016).
- ²⁴ S. Chambon, L. Derue, M. Lahaye, B. Pavageau, L. Hirsch and G. Wantz, “MoO₃ Thickness, Thermal Annealing and Solvent Annealing Effects on Inverted and Direct Polymer Photovoltaic Solar Cells,” *Materials* **5**, 2521–2536 (2012).
- ²⁵ A. M. Goodman and A. Rose “Double Extraction of Uniformly Generated Electron-Hole Pairs from Insulators with Noninjecting Contacts,” *J. Appl. Phys.* **42**, 2823(1971).
- ²⁶ M. O. Reese, S. A. Gevorgyan, M. Jørgensen, E. Bundgaard, S. R. Kurtz, D. S. Ginley, D. C. Olson, M. T. Lloyd, P. Morvillo, E. A. Katz, A. Elschner, O. Haillant, T. R. Currier, ... F. C. Krebs, “Consensus Stability Testing Protocols for Organic Photovoltaic Materials and Devices,” *Sol. Energy Mater Sol. Cells* **95**, 1253–1267 (2010).

- ²⁷ W. Greenbank, L. Hirsch, G. Wantz and S. Chambon, “Interfacial Thermal Degradation in Inverted Organic Solar Cells,” *Appl. Phys. Lett.* **107**, 263301 (2015).
- ²⁸ Y. Busby, E. J. W. List-Kratochvil and J.-J. Pireaux, “Chemical Analysis of the Interface in Bulk-Heterojunction Solar Cells by X-ray Photoelectron Spectroscopy Depth Profiling,” *ACS Appl. Mater. Interfaces* **9**, 3842–3848 (2017).
- ²⁹ F. Matteocci, Y. Busby, J.-J. Pireaux, G. Divitini, S. Cacovich, C. Ducati and A. Di Carlo, “Interface and Composition Analysis on Perovskite Solar Cells,” *ACS Appl. Mater. Interfaces* **7**, 26176–26183 (2015).
- ³⁰ X. Li, K. A. Wepasnick, X. Tang, Y. Wang, K. H. Bowen, D. H. Fairbrother and G. Gantefoer, “Ion Induced Modification of Size-Selected MoO₃ and WO₃ Clusters Deposited on HOPG,” *J. Vac. Sci. Technol. B* **30**, 31806 (2012).
- ³¹ H. Simchi, B. E. McCandless, T. Meng and W. N. Shafarman, “Structure and Interface Chemistry of MoO₃ Back Contacts in Cu(In,Ga)Se₂ Thin Film Solar Cells,” *J. Appl. Phys.* **115**, 033514 (2014).
- ³² G. Nagy and A. V. Walker, “Dynamics of Reactive Metal Adsorption on Organic Thin Films,” *J. Phys. Chem. C* **111**, 8543–8556 (2007).
- ³³ L. Chang, H. W. A. Lademann, J. B. Bonekamp, K. Meerholz, and A. J. Moulé, “Effect of Trace Solvent on the Morphology of P3HT:PCBM Bulk Heterojunction Solar Cells”. *Adv. Funct. Mater.* **21**, 1779–1787 (2011).
- ³⁴ W. C. Tsoi, S. J. Spencer, L. Yang, A. M. Ballantyne, P. G. Nicholson, A. Turnbull, A. G. Shard, C. E. Murphy, D. D. C. Bradley, J. Nelson and J. Kim, ”Effect of Crystallization on

- the Electronic Energy Levels and Thin Film Morphology of P3HT: PCBM Blends,” *Macromolecules* **44**, 2944–2952 (2011).
- ³⁵ B. Kadem, A. Hassan, and W. Cranton, “Efficient P3HT:PCBM Bulk Heterojunction Organic Solar cells; Effect of Post Deposition Thermal Treatment,” *J. Mater. Sci.: Mater. Electron* **27**, 7038–7048 (2016).
- ³⁶ W. Wang, S. Guo, E. M. Herzig, K. Sarkar, M. Schindler, D. Magerl, M. Philipp, J. Perlich and P. Müller-Buschbaum, “Investigation of Morphological Degradation of P3HT:PCBM Bulk Heterojunction Films Exposed to Long-Term Host Solvent Vapor,” *J. Mater. Chem. A* **4**, 3743–3753 (2016).
- ³⁷ S. A. Dowland, M. Salvador, J. D. Perea, N. Gasparini, S. Langner, S. Rajoelson, H. H. Ramanitra, B. D. Lindner, A. Osvet, C. J. Brabec, R. C. Hiorns and H. J. Egelhaaf, “Suppression of Thermally Induced Fullerene Aggregation in Polyfullerene-Based Multiacceptor Organic Solar Cells,” *ACS Appl. Mater. Interfaces* **9**, 10971–10982 (2017).
- ³⁸ H. H. Ramanitra, S. A. Dowland, B. A. Bregadiolli, M. Salvador, H. Santos Silva, D. Bégué, C. F. O. Graeff, H. Peisert, T. Chassé, S. Rajoeleson, A. Osvet, C. J. Brabec, H. J. Egelhaaf, ... R. C. Hiorns, “Increased Thermal Stabilization of Polymer Photovoltaic Cells with Oligomeric PCBM,” *J. Mater. Chem. C* **4**, 8121–8129 (2016).
- ³⁹ A. L. Ayzner, C. J. Tassone, S. H. Tolbert and B. J. Schwartz, “Reappraising the Need for Bulk Heterojunctions in Polymer - Fullerene Photovoltaics : The Role of Carrier Transport in All-Solution-Processed P3HT / PCBM Bilayer Solar Cells,” *J. Phys. Chem. C* **113**, 20050–20060 (2009).

- ⁴⁰ J. H. Park, J. S. Kim, J. H. Lee, W. H. Lee and K. Cho, “Effect of Annealing Solvent Solubility on the Performance of Poly(3-Hexylthiophene)/Methanofullerene Solar Cells,” *J. Phys. Chem. C* **113**, 17579–17584 (2009).
- ⁴¹ V. D. Mihailetschi, L. J. A. Koster, J. C. Hummelen and P. W. Blom, “Photocurrent Generation in Polymer-Fullerene Bulk Heterojunctions,” *Phys. Rev. Lett.* **93**, 19–22 (2004).
- ⁴² H. Azimi, A. Senes, M. C. Scharber, K. Hingerl and C. J. Brabec, “Charge Transport and Recombination in Low-Bandgap Bulk Heterojunction Solar Cell Using Bis-Adduct Fullerene,” *Adv. Energy Mater.* **1**, 1162–1168 (2011).
- ⁴³ S. Noh, C. K. Suman, D. Lee, S. Kim and C. Lee, “Study of Buffer Layer Thickness on Bulk Heterojunction Solar Cell,” *J. Nanosci. Nanotechnol.* **10**, 6815–6818 (2010).
- ⁴⁴ T. Stubhan, T. Ameri, M. Salinas, J. Krantz, F. MacHui, M. Halik and C. J. Brabec, “High Shunt Resistance in Polymer Solar Cells Comprising a MoO₃ Hole Extraction Layer Processed from Nanoparticle Suspension,” *Appl. Phys. Lett.* **98**, 253308 (2011).
- ⁴⁵ J. Reinhardt, M. Grein, C. Bühler, M. Schubert and U. Würfel, “Identifying the Impact of Surface Recombination at Electrodes in Organic Solar Cells by means of Electroluminescence and Modeling,” *Adv. Energy Mater.* **4**, 1400081 (2014).
- ⁴⁶ M. T. Greiner, L. Chai, M. G. Helander, W. M. Tang and Z. H. Lu, “Metal/Metal-Oxide Interfaces: How Metal Contacts Affect the Work Function and Band Structure of MoO₃,” *Adv. Funct. Mater.* **23**, 215–226 (2013).

- ⁴⁷ S. R. Cowan, A. Roy and A. J. Heeger, "Recombination in Polymer-Fullerene Bulk Heterojunction Solar Cells," *Phys. Rev. B* **82**, 245207 (2010).
- ⁴⁸ M. Limpinsel, A. Wagenpfahl, M. Mingeback, and C. Deibel, "Photocurrent in Bulk Heterojunction Solar Cells," *Phys. Rev B* **81**, 085203 (2010).
- ⁴⁹ L. Onsager, "Deviations from Ohm's Law in Weak Electrolytes," *J. Phys. Chem.* **2**, 599 (1934).
- ⁵⁰ C. L. Braun, "Electric Field Assisted Dissociation of Charge Transfer States as a Mechanism of Photocarrier Production," *J. Phys. Chem.* **80**, 4157 (1984).
- ⁵¹ R. Sokel and R. C. Hughes, "Numerical analysis of transient photoconductivity in insulators," *J. Appl. Phys.* **53**, 7412 (1984).
- ⁵² E. Siebert-Henze, V. G. Lyssenko, J. Fischer, M. Tietze, R. Brueckner, M. Schwarze, K. Vandewal, D. Ray, M. Riede and K. Leo, "Built-in Voltage of Organic Bulk Heterojunction p-i-n Solar Cells measured by Electroabsorption Spectroscopy" *AIP Adv.* **4**, 047134 (2014).